Article

Coulomb-correlated electron number states in a transmission electron microscope beam

Rudolf Haindl [1,2], **Armin Feist** [1,2] ✉, **Till Domröse** [1,2], **Marcel Möller** [1,2], **John H. Gaida** [1,2], **Sergey V. Yalunin**[1,2] **& Claus Ropers** [1,2] ✉

While correlated electrons are at the heart of many phenomena in condensed matter, as well as atomic and molecular physics, Coulomb interactions in free-electron beams are generally considered detrimental. Here, we demonstrate the generation of Coulomb-correlated pair, triple and quadruple states of free electrons by femtosecond photoemission from a nanoscale field emitter inside a transmission electron microscope. Event-based electron spectroscopy allows the spatial and spectral characterization of the electron ensemble emitted by each laser pulse. We identify distinctive energy and momentum correlations arising from acceleration-enhanced interparticle energy exchange, revealing strong few-body Coulomb interactions at an energy scale of 2 eV. State-sorted beam caustics show a discrete increase in virtual source size and longitudinal source shift for few-electron states, associated with transverse momentum correlations. We observe field-controllable electron antibunching, attributed primarily to transverse Coulomb deflection. The pronounced spatial and spectral characteristics of these electron number states allow filtering schemes that control the statistical distribution of the pulse charge. In this way, the fraction of specific few-electron states can be actively suppressed or enhanced, facilitating the preparation of highly non-Poissonian electron beams for microscopy and lithography, including future heralding schemes and correlated multi-electron probing.

Correlations between electrons are at the core of numerous phenomena in atomic, molecular and solid-state physics. Mediated by the Coulomb force, few- and many-body electronic correlations govern intriguing phases of matter, such as superconductivity or charge ordering, and they underpin a wide variety of applications down to nanoscale single-electron sources[1,2] and logic gates based on single charges[3,4]. In contrast to the opportunities offered by electron correlations in condensed matter, Coulomb interactions in free-electron beams are usually considered to have adverse effects. In electron microscopy, electron repulsion leads to stochastic longitudinal and transverse emittance growth of the beam, described by the Boersch[5] and Loeffler[6] effects, respectively, and limiting the brightness of state-of-the-art

electron sources[7,8]. In high-charge electron pulses for time-resolved experiments, mean-field and stochastic Coulomb effects govern the achievable pulse duration, energy spread and focusability, and pose a major experimental challenge for ultrafast electron diffraction[9–14] and microscopy[15–17], particle accelerators[18] and free-electron lasers[19].

Studying strong electronic correlations in a beam containing only a few particles requires the preparation of a sufficient electron phase space degeneracy. Field emitters represent highly localized sources, and they have been used in studies elucidating free-electron correlations[20–22]. In particular, the physical origin of antibunching in free-electron beams, as reported by Kiesel et al.[20], has been a long-standing question and is still actively discussed in the context of

[1]Max Planck Institute for Multidisciplinary Sciences, Göttingen, Germany. [2]4th Physical Institute - Solids and Nanostructures, University of Göttingen, Göttingen, Germany. ✉e-mail: armin.feist@mpinat.mpg.de; claus.ropers@mpinat.mpg.de
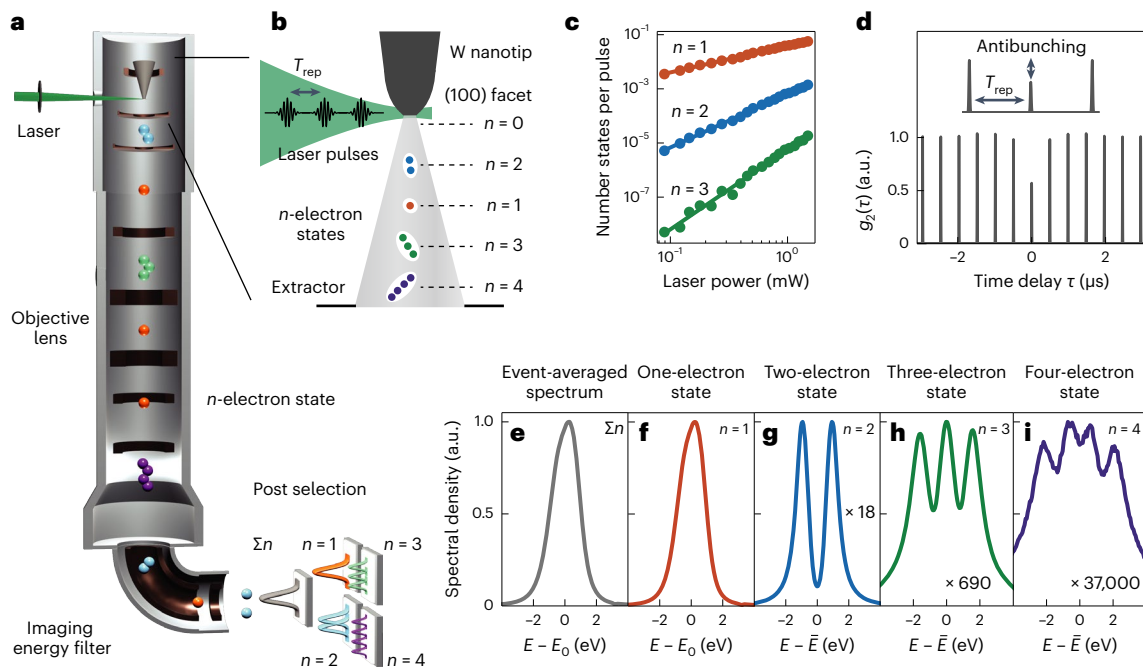
Fig. 1 | Electron number states in event-based transmission electron microscopy. a, Experimental setup. Few-electron states are prepared by pulsed photoemission. The electrons pass the sample plane of the microscope and, via post selection, event-based electron spectroscopy enables number-state-selective beam analysis. **b**, Ultrashort electron pulses are emitted from a laser-assisted Schottky field emitter (W(100)/ZrO nanotip), with a pulse charge of up to a few electrons coupled to the microscope column. **c**, Power scaling of the rates of one-, two- and three-electron states with fitted slopes of 0.99 ($n = 1$), 1.99 ($n = 2$) and 2.95 ($n = 3$) on a double-logarithmic scale. **d**, Second-order correlation function $g_2(\tau)$ of detected electrons with a timing resolution of approximately 10 ns. Inset: The peaks are spaced by the repetition time between laser pulses T_{rep}. The strongly reduced correlation function at zero delay is a clear experimental signature of antibunching. **e**–**i**, The event-averaged spectrum (**e**) and separate number-state resolved contributions for $n = 1$ (**f**), $n = 2$ (**g**), $n = 3$ (**h**) and $n = 4$ (**i**). The two-, three- and four-electron spectra are magnified (see factors in panels) and show distinct shapes with n peaks, indicating discrete energetic separation.

exchange-mediated[21] and Coulomb[23,24] interactions. Tailoring such correlations in free-electron beams facilitates sub-Poissonian beam statistics[22], promising shot-noise-reduced imaging and lithography. Strong interparticle interactions are enabled by spatiotemporally confined femtosecond-pulsed photoemission from nanotips[25–32], employed for ultrafast electron microscopy and diffraction with high-coherence beams[13,16,33]. The pulse-averaged effects of Coulomb interactions from such sources have recently been investigated, and are associated with spectral broadening and a loss of temporal and spatial resolution[17,34–36].

Employing concepts from quantum optics[37], correlations among free electrons have previously been identified by coincidence detection using detector pairs[20–22,38], as in atomic and molecular science measuring electrons and ions[39,40], correlated photoemission[41–43] and ionization[44,45].

In electron microscopy, the recent advent of pixelated event detectors has substantially broadened capabilities for coincidence measurements involving electrons, as demonstrated for electron-correlated X-ray emission[46], cathodoluminescence at nanomaterials[47] and integrated photonic resonators[48]. These capabilities will foster the emerging area of free-electron quantum optics, promising quantum coherent manipulation[49–54] and sensing[55,56] at the nanoscale, and facilitating concepts based on electron–electron[20,57–59] or electron–light entanglement[48,57,59–62]. Establishing such schemes will require a fundamental and quantitative understanding of correlations between the single electrons in the beam.

Here, we demonstrate strong Coulomb correlations in few-electron states generated at a laser-driven Schottky field emitter. Using event-based electron spectroscopy and imaging, the kinetic energy distributions of electron ensembles emitted by single laser pulses are recorded, and events are sorted by the number of free electrons. Characteristic multi-lobed spectra for events containing two, three

and four electrons are found. We quantitatively characterize interparticle correlations in terms of both energy and transverse momentum, and observe that these few-body interactions dominate over mean-field (space charge) effects. Two-electron energy correlation functions reveal pronounced peaks separated by energy differences of around 1.7 eV, illustrating an energy exchange facilitated by acceleration-enhanced longitudinal interaction along the beam axis. Transverse correlations in conjunction with transverse momentum selection cause antibunching and sub-Poissonian beam statistics. The relative contributions of longitudinal and transverse correlations, and thus the resulting antibunching factor, can be controlled by the initial acceleration field. The findings shed light on fundamental correlations in multi-electron pulses and enable statistical control of electron beams for on-demand correlated few-particle imaging and spectroscopy.

The experiments presented in this study were carried out at the Göttingen Ultrafast Transmission Electron Microscope (see sketch in Fig. 1a)[16]. Using a femtosecond laser source, ultrashort electron pulse trains at low pulse charge are generated by near-threshold laser-assisted Schottky emission from a W(100)/ZrO emitter. After propagation through the column of the microscope, the electrons are detected with an event-based camera. The temporal resolution of the electron detector allows consecutive incident electron pulses to be distinguished, providing an unambiguous measure of the number n of transmitted electrons for each laser pulse (Fig. 1a,b).

The rates of n-electron events as a function of incident laser power are displayed in Fig. 1c. Specifically, the rate of single-electron emission scales linearly with power, in agreement with the employed process of near-threshold laser-assisted Schottky photoemission[16,63,64]. Correspondingly, the $n = 2$ and $n = 3$ electron rates scale with to the power of n; that is, with the square and cube, respectively, of the laser power (only one measurement at high power was conducted for $n = 4$).
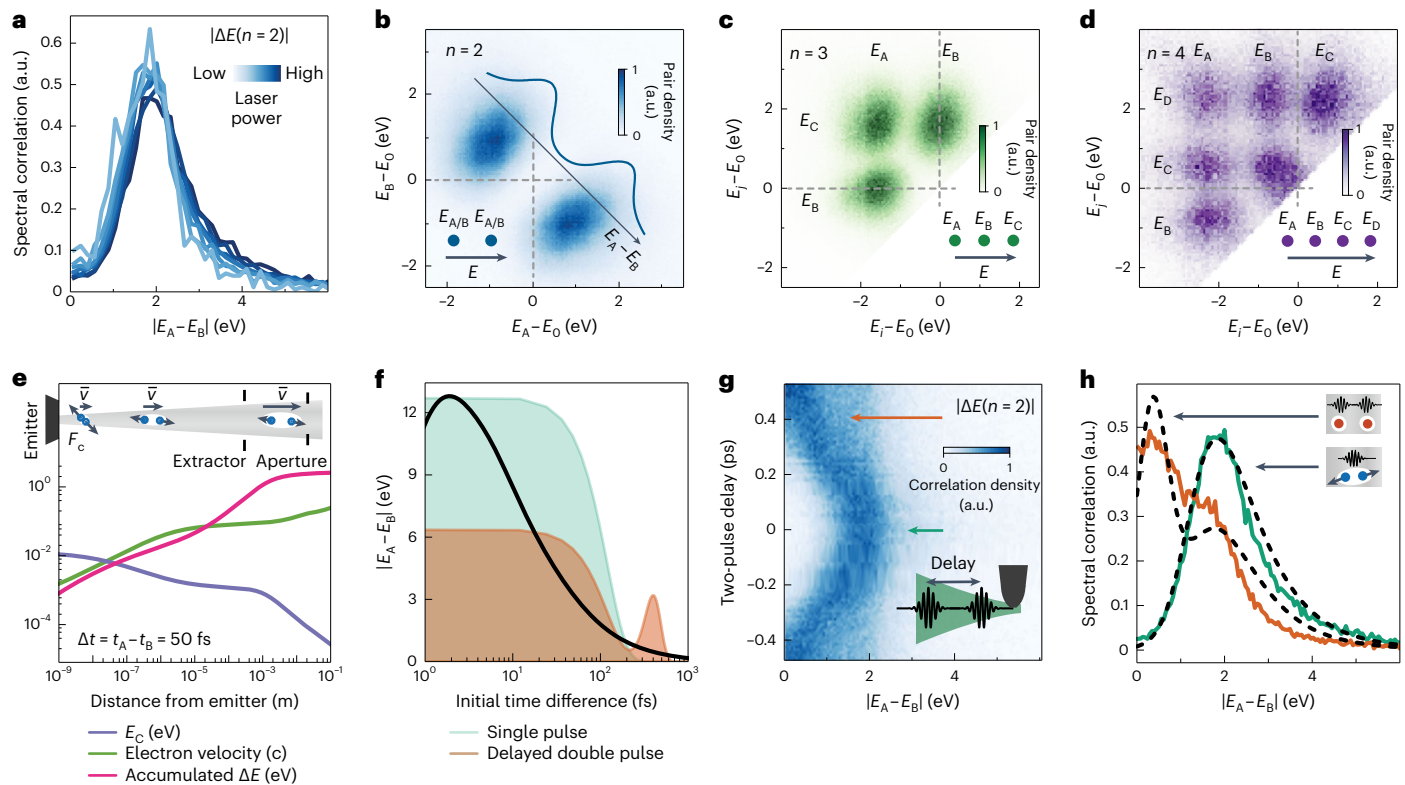
Fig. 2 | Coulomb-correlated few-electron pulses. a, The peak position of normalized one-sided pair correlation functions ($n = 2$) is nearly constant for varying laser power. **b**, Energy histogram of coincident $n = 2$ state electron pairs revealing a strong correlation in kinetic energy that is visible in the spectral correlation function (inset, integrated along the diagonal). **c,d**, The sorted energy histograms of $n = 3$ states (**c**) and $n = 4$ states (**d**) show clearly separated energy-pair correlation peaks of combinations E_i; E_{A-C} and E_j; E_{B-D}. **e**, Top: classical simulation scheme in a geometry consisting of emitter, extraction anode, second acceleration stage and aperture. Two electrons (blue dots) at the nanotip are injected into the static field with a temporal separation of $\Delta t = 50$ fs and are repelled by the inter-particle Coulomb force F_C. Bottom: the momentary Coulomb energy E_C (purple), electron velocity (green) and accumulated energy

difference ΔE (magenta) are plotted against the electron travel distance from the emitter. A small initial Coulomb energy translates to a greatly enhanced final energy difference during acceleration. **f**, Final two-electron energy separations for varying emission time differences. The distributions of emission time differences for two Gaussian pulse shapes with a full-width-at-half-maximum of 200 fs at delays of 0 ps (green) and 0.4 ps (orange) are shown by the shaded regions. **g**, Pair correlation density of $n = 2$ states (colour scale) for photoemission with two delayed laser pulses. A strong correlation gap is observed at temporal overlap that gradually disappears for pulse delays >200 fs. The coloured arrows correspond to spectra in **h**. **h**, Comparison of pulse pair correlation spectra from **g** at temporal overlap (green) and a delay of 0.4 ps (orange) with simulated correlation spectra (dashed lines).

Considering the relative distribution of n-electron events at a given laser power, we identify sub-Poissonian statistics. Specifically, defining P_1 as the probability of detecting one electron in a pulse, a Poisson process predicts a probability of $P_n = P_1^n/n!$ of detecting n electrons. The actual rates measured for $n = 2$ and $n = 3$ are lower, at only 85% and 57%, respectively, of those expected from the single-electron rate. This antibunching is also evident from a dip in the second-order correlation function at time delay $\tau = 0$ (Fig. 1d), as discussed in detail below.

We next investigate the kinetic energies of these number-sorted electron states (Fig. 1e–i). The spectral distribution of the one-electron events (Fig. 1f), which also dominates the total spectrum (Fig. 1e, summed over all events), consists of a single peak centred on the acceleration energy of $E_0 = 200$ keV. In stark contrast, the spectra of the few-electron events exhibit a number of lobes identical to the number of particles contained. In Fig. 1g–i, we plot the spectral distributions of the electron events sorted into event classes $n = 2, 3, 4$ with respect to the average energy $\bar{E}$ of the electrons in each pulse. Extended Data Fig. 1 shows the spectra of the event classes with respect to the acceleration energy.

For the $n = 2$ events, this results in a histogram of energy differences—that is, the energy correlation function of the two-electron state. Depicted in terms of the magnitude of the energy difference in Fig. 2a, these measurements reveal a clear correlation gap of the energies of

both electrons in a $n = 2$ state. A natural assumption would be that this energy gap arises from Coulomb interactions. A first question that needs to be answered is to what degree these correlations are modified by emitted electrons near the source that are not transmitted to the column, as such electrons are known to affect the overall spectral distribution[7,8,15–17,65,66]. We find that the correlation function is only weakly dependent on the laser power, and thus the average number of electrons (Extended Data Fig. 2). This shows that we are observing an effect that is governed primarily by the interaction of those few electrons within the measured ensemble.

The measurement scheme allows us to analyse the spectral characteristics in terms of two-dimensional energy correlation functions. Figure 2b shows the pair density distribution as a function of the electron energies E_A and E_B associated with two electrons A and B in the same electron pulse. The pairs exhibit a strong correlation gap around zero energy difference $E_A - E_B$. The broadening of the pair distribution in the average energy $(E_A + E_B)/2$ is found to depend more strongly on the laser power, illustrating that both electrons are affected jointly by an increase in stochastic interactions with electrons not entering the column (Methods). An analysis of the pair distribution of electron energies for the cases of $n = 3$ and $n = 4$ electrons (Fig. 2c,d) strikingly demonstrates a persistent, regular arrangement of the energies of electrons produced in a single pulse. These measurements highlight

the pronounced interparticle Coulomb correlation at the level of 1–2 eV per electron, which we study further below.

To elucidate the physical origins of these strong correlations, we numerically simulate the particle propagation including the static acceleration field and interparticle Coulomb interactions. Specifically, we compute trajectories for sets of electrons with initial conditions representing the emission at the tip in terms of the distributions of initial momentum, emission location and temporal separation. Experimental parameters for the acceleration voltages and approximate electrode distances are used in the simulations, with further details provided in Supplementary Section C.

The most important findings of the simulations are a quantitative prediction and rationalization of the magnitude of the observed Coulomb correlations. Figure 2e illustrates the simulation result for an individual pair of electrons emitted with typical parameters for our experimental conditions. The electrons are extracted from the source with spatial and temporal separations of 8 nm and 50 fs, respectively. At the moment of emission of the second electron, the surface electric field of 0.5 V m⁻¹ has already accelerated the first electron to a distance of 130 nm from the emitter surface, such that the initial transverse separation only accounts for a small fraction of the total particle distance. The electrostatic Coulomb energy at the time of emission of the second electron amounts to only 12 meV. Thus, the question of how such small electrostatic energies can translate to a final energy difference of 2 eV and higher arises.

We first provide a qualitative explanation of the enhanced correlation, using non-relativistic expressions for simplicity. In the absence of an accelerating field and for particles with mass m initially at rest, the Coulomb energy E_C would only translate to a velocity difference of $\Delta v = v_A - v_B = 2\sqrt{E_C/m}$. However, considering the external acceleration of the particles to a mean velocity $\bar{v} = (v_A + v_B)/2$, the same velocity difference results in a kinetic energy difference $\propto \bar{v}\Delta v$ that is substantially larger than E_C (see also ref. 67). Moreover, Coulomb energy is transferred to high kinetic energy differences only while the electrons are already at higher velocity in the laboratory frame. In particular, for $\bar{v} \gg \Delta v$, the rate of energy exchange of the electrons is approximated as the product of the momentary interparticle Coulomb force and the centre-of-mass velocity in the laboratory frame (that is, $P = F_C\bar{v}$). The final energy difference then becomes $\Delta E = \int dt P(t)$. Therefore, the nearly negligible initial Coulomb energy is magnified by the continuous centre-of-mass acceleration to a large final energy difference.

In Fig. 2e, the kinetic energy difference (magenta), interparticle Coulomb energy (purple) and momentary electron velocity (green) of the second particle are plotted on a double-logarithmic scale as a function of the distance of this particle from the emitter surface. It is evident that a few-hundred-millielectronvolt energy separation emerges on propagation to the extractor electrode in the electrostatic gun, while a further increase in the final energy difference of nearly 2 eV for these particles requires propagation and acceleration over several more millimetres. We note that by using a controlled femtosecond gate, this scenario represents a maximally controlled limit of the stochastic Coulomb interactions in the initial acceleration stages of electron microscopes[67,68], first addressed by Boersch[5] and Loeffler[6].

The simulations also yield further insight into the characteristic timescales over which this electron–electron correlation persists. Figure 2f displays the computed final energy difference as a function of the initial temporal separation of two electrons (black solid line). We find that the energy difference drops to about 1 eV within 200 fs. As the laser pulse acts as a temporal gate for the photoemission, a prediction of the energy correlation function is obtained from these computed energy separations, weighted by the distribution of emission time differences under the photoemission laser pulse envelope (shaded area). The gap then arises from the fact that the laser pulse duration of ~150 fs does not lead to a substantial fraction of electron pairs with a larger separation in emission time. We experimentally probe this
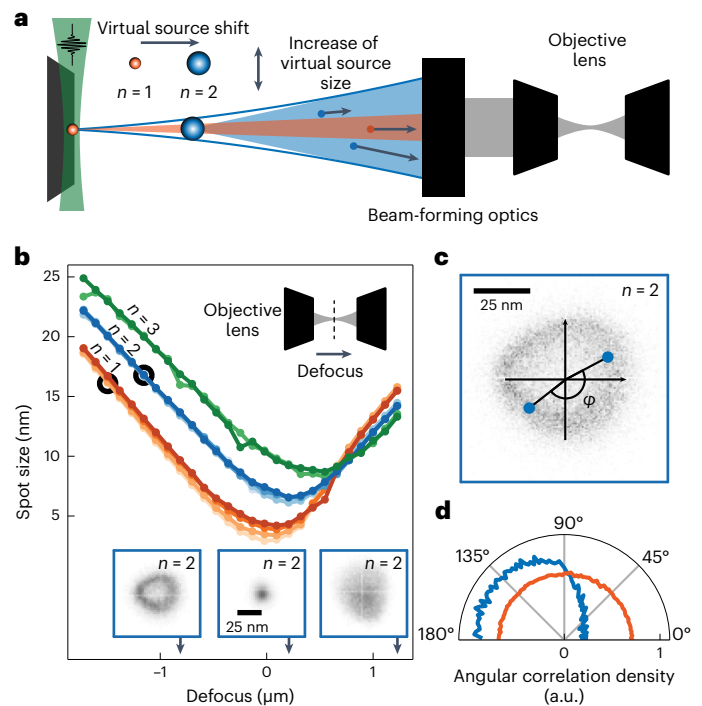
interpretation by conducting measurements using a pair of laser pulses of variable delays (Fig. 2g). The measured correlation gap closes for a temporal separation of the two laser pulses longer than 200 fs. Beyond such delays, an increasing number of electrons with small energy differences and near the central energy of the beam are found, and for those events, one electron is emitted in each pulse. A direct comparison of the experimental and simulated energy correlation functions for pulse overlap and for 0.4 ps two-pulse delays (Fig. 2h) yields convincing agreement. We also find excellent agreement with simulations for $n = 3, 4$ states (Extended Data Fig. 3).

Alongside their spectral distributions and correlations, the few-electron states observed here possess characteristic spatial properties. Specifically, in Fig. 3b, we show n-dependent beam caustics, which exhibit discrete differences in both the minimum spot size and focal position. Variations in the laser power yield changes in the caustics (higher power leads to some increase in spot size), but are far less pronounced than the differences between the event classes. Under the given conditions, the focusability is limited by spherical aberrations of the objective lens and the virtual source size, which result in typical spot profiles for positive and negative defocus (inset in Fig. 3b). The $n > 1$ caustics are evidently the result of a larger effective source, and the beam waist is shifted towards positive defocus.

Both observations can be understood from mutual transverse deflection (sketch in Fig. 3a), which laterally spreads the few-electron trajectories[17] such that the virtual source increases in size and moves forwards, as predicted in simulations[36,38].

Fig. 3 | Characterization of the spatial electron beam properties. a, Schematic of the effect of Coulomb interactions on an electron beam coupled to an electron microscope. The virtual source increases in size and is shifted along the electron beam axis for pulse charges of two and three electrons. **b**, Caustics of the electron beam sorted by n, recorded by varying the last condenser lens of the microscope (light colours correspond to low power, dark colours to high power). The insets are images of the beam profile in underfocus (left), focus (middle) and overfocus (right) for $n = 2$ (blue outlines). **c**, Image of the $n = 2$-beam profile in underfocus, and the correlation angle φ between electron pairs with respect to the beam centre. The underfocus condition allows a precise measurement of the angular correlation. **d**, A strong anisotropic angular correlation is observed for $n = 2$ compared with an isotropic distribution for drawing random events from the $n = 1$ event class. The datasets employed are indicated by black circles around the data points in **b**.

A more detailed view of the spatial properties of few-electron states is obtained by analysing correlations in the transverse momentum. To this end, we measure position correlations for a sufficiently large negative defocus (Fig. 3c). The spatial correlation is quantified via the angle φ between the two electrons and the beam centre. Figure 3d shows the angular correlation density of the two-electron state compared with random correlations drawn from a corresponding single-electron state at the same spot size (15 nm). In the electron pair state, we obtain a strong anisotropic correlation with a maximum around an angle of 180°, corresponding to electron events localized on opposite sides of the defocused beam, and thus exhibiting nearly opposite transverse momenta. Moreover, the angular correlation becomes most pronounced for events with the largest transverse momentum (Extended Data Fig. 4).

These observations clearly demonstrate that two-particle Coulomb interactions induce pronounced correlations in both the longitudinal and transverse momenta of the electrons. As the correlation primarily emerges in the initial acceleration stages of the electron gun, we explore the extent to which they can be controlled by the extraction fields. Qualitatively, a larger acceleration field is expected to enhance the longitudinal correlations and large kinetic energy differences in the beam direction, while a weaker acceleration allows the electrons to exchange more transverse momentum while limiting the growth of the final energy difference. Figure 4a sketches this trade-off between longitudinal and transverse correlations, which manifests experimentally in distinct properties of the few-electron states. Specifically, a decrease in the extraction voltage (that is, in the potential difference applied between the tip and the first anode) substantially reduces the observed energy correlation gap and the slope of the high-energy tail (Fig. 4b, solid lines; crosses in Fig. 4d denote the peak of the correlation function). Both features are reproduced in the two-particle simulations described earlier (Fig. 4b, dashed lines).

Interestingly, the enhanced transverse interaction at lower extraction fields has an immediate impact on the statistical distribution of the electron number states. Specifically, the measured beam caustics in Fig. 3b show that the convergence angle and thus the maximum transverse momentum of the individual particles is the same for all event classes, irrespective of n, primarily limited by the microscope's condenser aperture. Therefore, the additional transverse momentum gained by Coulomb repulsion leads to a loss of total transmission of electron pairs. The corresponding change in the statistical distribution of events is expressed in terms of the second-order (current–current) correlation function $g_2(\tau)$ as a function of the delay τ between recorded electrons, shown in Fig. 4c. We see that the emitted charge in sequential pulses is statistically independent ($g_2(\tau) \approx 1$), while clear antibunching is observed for the electrons recorded from a single pulse ($g_2(0) < 1$). In other words, at $U_{ext} = 400$ V, the probability of detecting $n = 2$ electrons is reduced by a factor of $1 - g_2(0) = 0.43$ compared with a Poissonian process with the same average electron number per pulse. Importantly, we determine that the antibunching becomes much more pronounced for a smaller extraction voltage (Fig. 4d, circles), illustrating that the enhanced transverse correlations leads to a loss of pairs in the beam path by momentum-selective transmission. As in the case of the energy correlation, the controlled femtosecond temporal gate enabled by photoemission facilitates such strong antibunching[22], which is orders of magnitude larger than has been observed for continuous[20,38] and nanosecond-pulsed[21] electron microscope beams.

Although the employed event-based measurements in conjunction with photoemission gating reveal important aspects of these few-particle correlations, it should be noted that the same phenomena will contribute to the properties of conventional (continuous) electron beams, with direct ramifications for the total beam brightness, coherence and non-correctable stochastic aberrations. However, in turn, the specific knowledge of these correlations allows control of the number statistics in the photoemitted beam, which may directly
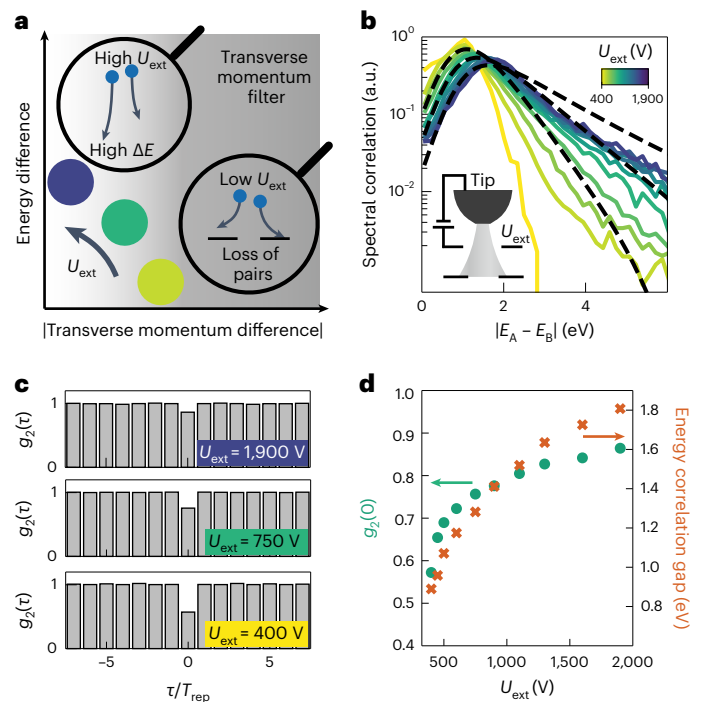
Fig. 4 | Electric-field control of longitudinal versus transverse correlations. a, Via the extraction voltage, U_{ext}, the initial acceleration serves as a control parameter to favour either energy or transverse momentum separation in the doublet states. Electron optical elements act as transverse momentum filters (background shading) and lead to lower transmission of electron pairs for weaker initial acceleration (low U_{ext}). **b**, Electron pair correlation functions for varying extraction voltage. Particle tracking simulations (dashed lines) agree with the observed changes in correlation gap with U_{ext}. The inset shows a schematic of the electron optics with emitter, extractor and aperture. **c**, Delay-dependent current–current correlation function $g_2(\tau)$ for $U_{ext} = 1,900, 750, 400$ V. The suppression at zero delay ($g_2(0)$) is most pronounced for low U_{ext}. **d**, $g_2(0)$ (left y axis) and energy correlation gap (right y axis) versus U_{ext}.

benefit microscopy applications. The antibunching observed here and in recent work[22] implies that the total photocurrent exhibits sub-Poissonian noise characteristics—a property that is highly sought after in condensed matter scenarios (for example, as achieved by Coulomb blockade[69]). In the context of electron microscopy, this feature could be directly applied for shot-noise reduction in imaging and lithography, with immediate consequences for low-dose applications owing to the possibility of avoiding multi-electron specimen damage. In fact, our findings may be directly relevant for the mechanisms underlying the recently observed reduction in sample degradation with pulsed beams[70,71]. Further potential arises from the strong Coulomb correlations in energy and momentum identified for the few-electron states. For example, the fact that both electrons in the doublet state are well separated in energy and transverse momentum from each other allows for an energetic or spatial selection of the respective number state. This facilitates a powerful approach to controlling the statistics of single- and double-electron events.

In particular, the analysis of the measured spot profiles shows that a spatial aperture in a beam cross-over could be used to selectively favour the transmission T_1 of the $n = 1$ number state by a factor of 3 and nearly 8 over the transmissions T_2 and T_3 of the $n = 2$ and $n = 3$ states, respectively (Fig. 5a,b). Similarly, a pre-specimen energy filter commonly used in state-of-the-art electron microscopes[72] could be adjusted to enhance the transmission probability of $n = 1$ compared with $n = 2$ states (Fig. 5c). Specifically, for experimentally measured single-electron and double-electron spectra (Fig. 5e), the $n = 1$ transmission probability exceeds the $n = 2$ transmission probability by a factor of 8 at small slit
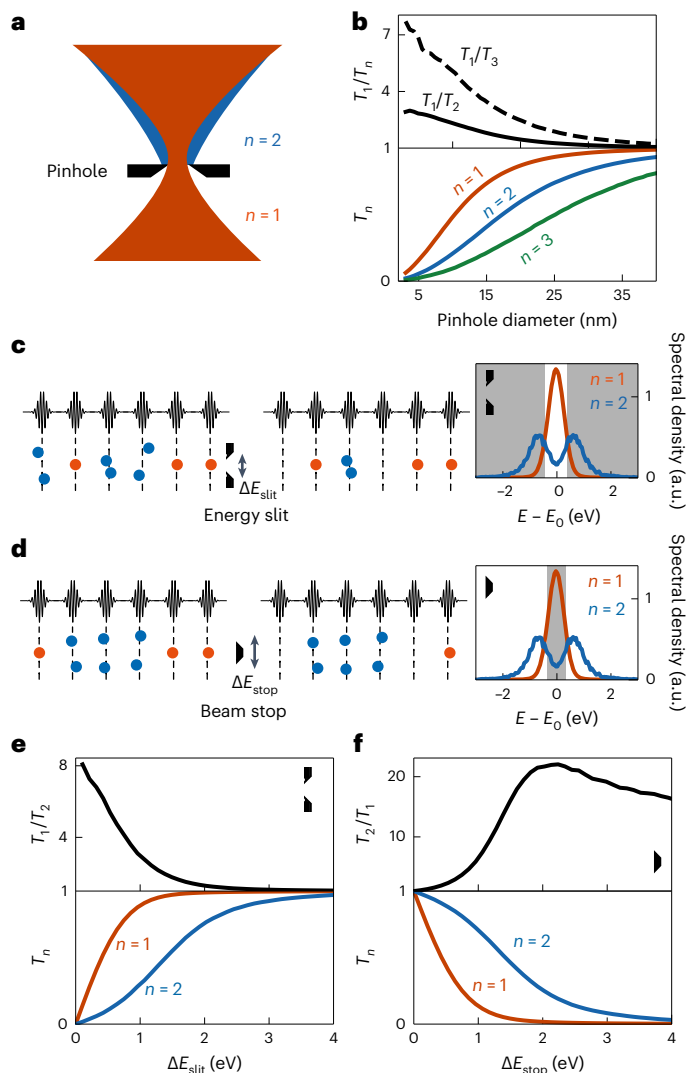
Fig. 5 | Statistical control of single- and double-electron states using spatial and spectral filtering. a, A pinhole positioned at the beam waist of the $n = 1$ beam profile spatially filters higher-number states. **b**, State-selective beam transmissions T_n (bottom, calculated from data in Fig. 3) and transmission ratios T_1/T_2 and T_1/T_3, with increased relative selectivity of the $n = 1$ electron state (top). **c**,**d**, Left: in a spectrally dispersed plane, an energy-selective slit (energy width ΔE_{slit}) reduces the transmission of $n = 2$ electron states (**c**), whereas an energy beam stop (energy width ΔE_{stop}) suppresses the $n = 1$ electron states, enhancing the transmission of $n = 2$ electron states (**d**). Right: experimental spectra of $n = 1$ and $n = 2$ electron states (grey shading indicates the spectral density rejected by the energy slit/beam stop). **e**,**f**, Transmission T_n (bottom) and transmission ratios T_1/T_2 and T_2/T_1 (top) for the scenarios in **c** (**e**) and **d** (**f**). Considering individually optimized energy windows, 8-fold and 20-fold enhanced state selectivities are found for $n = 1$ and $n = 2$, respectively.

widths, greatly amplifying the sub-Poissonian nature of the electron number distribution and facilitating a shot-noise-reduced electron current. Conversely, a central beam stop in energy could suppress a substantial fraction of single-electron states, leading to up to 20-fold enhancement of pair-state over $n = 1$ state transmissions (Fig. 5d,f). This approach will enable new forms of microscopy and spectroscopy with correlated electrons for a variety of two-point or two-time measurement schemes in correlated materials and free-electron quantum optics.

In conclusion, the highly correlated electron number states introduced in this work are of interest both for fundamental considerations and their potential utility in manifold electron beam applications.

For example, the pair state can be employed to implement a high-fidelity source of electron-heralded single electrons, enabling shot-noise-free imaging and lithography with a precisely counted number of electrons. Furthermore, the elementary scattering process that creates these well-defined few-body states might generally be assumed to induce entanglement between the electrons. Future studies may address the coherence of such multi-electron states and their possible use as free-electron qubits, with potential applications spanning from interaction-free or correlation-based quantum electron microscopy to quantum information processing.

Finally, we would like to note the study by S. Meier et al.[73] on energy correlations of photoelectron pairs emitted from a free-standing tungsten tip, printed as a companion paper in this issue.

Online content

Any methods, additional references, Nature Portfolio reporting summaries, source data, extended data, supplementary information, acknowledgements, peer review information; details of author contributions and competing interests; and statements of data and code availability are available at https://doi.org/10.1038/s41567-023-02067-7.

References

1. Fève, G. et al. An on-demand coherent single-electron source. *Science* **316**, 1169–1172 (2007).
2. Bocquillon, E. et al. Coherence and indistinguishability of single electrons emitted by independent sources. *Science* **339**, 1054–1057 (2013).
3. Kastner, M. A. The single-electron transistor. *Rev. Mod. Phys.* **64**, 849–858 (1992).
4. Zrenner, A. et al. Coherent properties of a two-level system based on a quantum-dot photodiode. *Nature* **418**, 612–614 (2002).
5. Boersch, H. Experimentelle Bestimmung der Energieverteilung in thermisch ausgelösten Elektronenstrahlen. *Z. Phys.* **139**, 115–146 (1954).
6. Loeffler, K. H. Energy-spread generation in electron-optical instruments. *Z. Angew. Phys.* **27**, 145 (1969).
7. Jansen, G. Coulomb interactions in particle beams. *Nucl. Instrum. Methods A* **298**, 496–504 (1990).
8. Cook, B., Verduin, T., Hagen, C. W. & Kruit, P. Brightness limitations of cold field emitters caused by Coulomb interactions. *J. Vac. Sci. Technol. B* **28**, C6C74–C6C79 (2010).
9. Siwick, B. J., Dwyer, J. R., Jordan, R. E. & Miller, R. J. D. Ultrafast electron optics: propagation dynamics of femtosecond electron packets. *J. Appl. Phys.* **92**, 1643–1648 (2002).
10. Collin, S. et al. Transverse and longitudinal space-charge-induced broadenings of ultrafast electron packets. *J. Appl. Phys.* **98**, 094910 (2005).
11. Michalik, A. M. & Sipe, J. E. Analytic model of electron pulse propagation in ultrafast electron diffraction experiments. *J. Appl. Phys.* **99**, 054908 (2006).
12. Reed, B. W. Femtosecond electron pulse propagation for ultrafast electron diffraction. *J. Appl. Phys.* **100**, 034916 (2006).
13. Paarmann, A. et al. Coherent femtosecond low-energy single-electron pulses for time-resolved diffraction and imaging: a numerical study. *J. Appl. Phys.* **112**, 113109 (2012).
14. Ischenko, A. A., Kochikov, I. V. & Miller, R. J. D. The effect of Coulomb repulsion on the space-time resolution limits for ultrafast electron diffraction. *J. Chem. Phys.* **150**, 054201 (2019).
15. Cook, B. & Kruit, P. Coulomb interactions in sharp tip pulsed photo field emitters. *Appl. Phys. Lett.* **109**, 151901 (2016).
16. Feist, A. et al. Ultrafast transmission electron microscopy using a laser-driven field emitter: femtosecond resolution with a high coherence electron beam. *Ultramicroscopy* **176**, 63–73 (2017).
17. Bach, N. et al. Coulomb interactions in high-coherence femtosecond electron pulses from tip emitters. *Struct. Dynam.* **6**, 014301 (2019).

18. Hofmann, I. *Space Charge Physics for Particle Accelerators* (Springer, 2017).

19. Emma, P., Huang, Z., Kim, K.-J. & Piot, P. Transverse-to-longitudinal emittance exchange to improve performance of high-gain free-electron lasers. *Phys. Rev. Spec. Top. Acc. Beams* **9**, 100702 (2006).

20. Kiesel, H., Renz, A. & Hasselbach, F. Observation of Hanbury Brown–Twiss anticorrelations for free electrons. *Nature* **418**, 392–394 (2002).

21. Kuwahara, M. et al. Intensity interference in a coherent spin-polarized electron beam. *Phys. Rev. Lett.* **126**, 125501 (2021).

22. Keramati, S., Brunner, W., Gay, T. J. & Batelaan, H. Non-Poissonian ultrashort nanoscale electron pulses. *Phys. Rev. Lett.* **127**, 180602 (2021).

23. Baym, G. & Shen, K. *Hanbury Brown–Twiss Interferometry with Electrons: Coulomb vs. Quantum Statistics* 201–210 (World Scientific, 2014).

24. Kodama, T. & Osakabe, N. Mechanism for correlation in a coherent electron beam. *Microscopy* **68**, 133–143 (2019).

25. Hommelhoff, P., Sortais, Y., Aghajani-Talesh, A. & Kasevich, M. A. Field emission tip as a nanometer source of free electron femtosecond pulses. *Phys. Rev. Lett.* **96**, 077401 (2006).

26. Ropers, C., Solli, D. R., Schulz, C. P., Lienau, C. & Elsaesser, T. Localized multiphoton emission of femtosecond electron pulses from metal nanotips. *Phys. Rev. Lett.* **98**, 043907 (2007).

27. Barwick, B. et al. Laser-induced ultrafast electron emission from a field emission tip. *New J. Phys.* **9**, 142 (2007).

28. Krüger, M., Schenk, M. & Hommelhoff, P. Attosecond control of electrons emitted from a nanoscale metal tip. *Nature* **475**, 78–81 (2011).

29. Herink, G., Solli, D. R., Gulde, M. & Ropers, C. Field-driven photoemission from nanostructures quenches the quiver motion. *Nature* **483**, 190–193 (2012).

30. Ciappina, M. F. et al. Attosecond physics at the nanoscale. *Rep. Progr. Phys.* **80**, 054401 (2017).

31. Seiffert, L., Paschen, T., Hommelhoff, P. & Fennel, T. High-order above-threshold photoemission from nanotips controlled with two-color laser fields. *J. Phys. B* **51**, 134001 (2018).

32. Dombi, P. et al. Strong-field nano-optics. *Rev. Mod. Phys.* **92**, 025003 (2020).

33. Houdellier, F., Caruso, G., Weber, S., Kociak, M. & Arbouet, A. Development of a high brightness ultrafast transmission electron microscope based on a laser-driven cold field emission source. *Ultramicroscopy* **186**, 128–138 (2018).

34. Yanagisawa, H. et al. Delayed electron emission in strong-field driven tunnelling from a metallic nanotip in the multi-electron regime. *Sci. Rep.* **6**, 35877 (2016).

35. Schötz, J. et al. Onset of charge interaction in strong-field photoemission from nanometric needle tips. *Nanophotonics* **10**, 3769–3775 (2021).

36. Meier, S. & Hommelhoff, P. Coulomb interactions and the spatial coherence of femtosecond nanometric electron pulses. *ACS Photon.* **9**, 3083–3088 (2022).

37. Mandel, L. & Wolf, E. *Optical Coherence and Quantum Optics* 1st edn (Cambridge Univ. Press, 1995).

38. Kodama, T., Osakabe, N. & Tonomura, A. Correlation in a coherent electron beam. *Phys. Rev. A* **83**, 063616 (2011).

39. Dörner, R. et al. Cold target recoil ion momentum spectroscopy: a 'momentum microscope' to view atomic collision dynamics. *Phys. Rep.* **330**, 95–192 (2000).

40. Ullrich, J. et al. Recoil-ion and electron momentum spectroscopy: reaction-microscopes. *Rep. Progr. Phys.* **66**, 1463–1545 (2003).

41. Muñoz-Navia, M. et al. Electron pair emission from a W(001) surface: photon versus electron excitation. *J. Phys. Condens. Matter* **21**, 355003 (2009).

42. van Riessen, G. et al. Direct and core-resonant double photo-emission from Cu(001). *J. Phys. Condens. Matter* **22**, 092201 (2010).

43. Trützschler, A. et al. Band-resolved double photoemission spectroscopy on correlated valence electron pairs in metals. *Phys. Rev. Lett.* **118**, 136401 (2017).

44. Larochelle, S., Talebpour, A. & Chin, S. L. Non-sequential multiple ionization of rare gas atoms in a Ti:sapphire laser field. *J. Phys. B* **31**, 1201–1214 (1998).

45. Becker, W., Liu, X., Ho, P. J. & Eberly, J. H. Theories of photoelectron correlation in laser-driven multiple atomic ionization. *Rev. Mod. Phys.* **84**, 1011–1043 (2012).

46. Jannis, D., Müller-Caspary, K., Béché, A., Oelsner, A. & Verbeeck, J. Spectroscopic coincidence experiments in transmission electron microscopy. *Appl. Phys. Lett.* **114**, 143101 (2019).

47. Varkentina, N. et al. Cathodoluminescence excitation spectroscopy: nanoscale imaging of excitation pathways. *Sci. Adv.* **8**, eabq4947 (2022).

48. Feist, A. et al. Cavity-mediated electron-photon pairs. *Science* **377**, 777–780 (2022).

49. Kfir, O., Di Giulio, V., de Abajo, F. J. G. & Ropers, C. Optical coherence transfer mediated by free electrons. *Sci. Adv.* **7**, eabf6380 (2021).

50. Asban, S. & García de Abajo, F. J. Generation, characterization, and manipulation of quantum correlations in electron beams. *npj Quant. Inf.* **7**, 42 (2021).

51. Zhao, Z., Sun, X.-Q. & Fan, S. Quantum entanglement and modulation enhancement of free-electron–bound-electron interaction. *Phys. Rev. Lett.* **126**, 233402 (2021).

52. Pan, Y. & Gover, A. Spontaneous and stimulated emissions of a preformed quantum free-electron wave function. *Phys. Rev. A* **99**, 052107 (2019).

53. Ben Hayun, A. et al. Shaping quantum photonic states using free electrons. *Sci. Adv.* **7**, eabe4270 (2021).

54. Rätzel, D., Hartley, D., Schwartz, O. & Haslinger, P. Controlling quantum systems with modulated electron beams. *Phys. Rev. Res.* **3**, 023247 (2021).

55. Di Giulio, V., Kociak, M. & de Abajo, F. J. G. Probing quantum optical excitations with fast electrons. *Optica* **6**, 1524–1534 (2019).

56. Tsarev, M., Ryabov, A. & Baum, P. Measurement of temporal coherence of free electrons by time-domain electron interferometry. *Phys. Rev. Lett.* **127**, 165501 (2021).

57. Kfir, O. Entanglements of electrons and cavity photons in the strong-coupling regime. *Phys. Rev. Lett.* **123**, 103602 (2019).

58. Talebi, N., & Březinová, I. Exchange-mediated mutual correlations and dephasing in free-electrons and light interactions. *New J. Phys.* **23**, 063066 (2021).

59. Konečná, A., Iyikanat, F. & García de Abajo, F. J. Entangling free electrons and optical excitations. *Sci. Adv.* **8**, eabo7853 (2022).

60. Rivera, N. & Kaminer, I. Light–matter interactions with photonic quasiparticles. *Nat. Rev. Phys.* **2**, 538–561 (2020).

61. García de Abajo, F. J. & Di Giulio, V. Optical excitations with electron beams: challenges and opportunities. *ACS Photon.* **8**, 945–974 (2021).

62. Taleb, M., Hentschel, M., Rossnagel, K., Giessen, H. & Talebi, N. Phase-locked photon–electron interaction without a laser. *Nat. Phys.* 1–8 (2023).

63. Cook, B., Bronsgeest, M., Hagen, K. & Kruit, P. Improving the energy spread and brightness of thermal-field (Schottky) emitters with PHAST—photo assisted Schottky tip. *Ultramicroscopy* **109**, 403–412 (2009).

64. Yang, D.-S., Mohammed, O. F. & Zewail, A. H. Scanning ultrafast electron microscopy. *Proc. Natl Acad. Sci. USA* **107**, 14993–14998 (2010).

65. Kuwahara, M. et al. The Boersch effect in a picosecond pulsed electron beam emitted from a semiconductor photocathode. *Appl. Phys. Lett.* **109**, 013108 (2016).

66. Bronsgeest, M. S., Barth, J. E., Schwind, G. A., Swanson, L. W. & Kruit, P. Extracting the Boersch effect contribution from experimental energy spread measurements for Schottky electron emitters. *J. Vac. Sci. Technol. B* **25**, 2049 (2007).

67. Kruit, P. & Jansen, G. H. In *Handbook of Charged Particle Optics*, 2nd edition, (ed Orloff, J.) 275–318 (CRC Press, 2009).

68. Jansen, G. H. *Coulomb Interactions in Particle Beams*. PhD thesis, Delft University of Technology (1988).

69. Alhassid, Y. The statistical theory of quantum dots. *Rev. Mod. Phys.* **72**, 895–968 (2000).

70. VandenBussche, E. J. & Flannigan, D. J. Reducing radiation damage in soft matter with femtosecond-timed single-electron packets. *Nano Lett.* **19**, 6687–6694 (2019).

71. Kisielowski, C. et al. Discovering hidden material properties of MgCl$_2$ at atomic resolution with structured temporal electron illumination of picosecond time resolution. *Adv. Funct. Mater.* **29**, 1807818 (2019).

72. Krivanek, O. L. et al. High-energy-resolution monochromator for aberration-corrected scanning transmission electron microscopy/electron energy-loss spectroscopy. *Phil. Trans. R. Soc. A* **367**, 3683–3697 (2009).

73. Meier, S., Heimerl, J. & Hommelhoff, P. Few-electron correlations after ultrafast photoemission from nanometric needle tips. *Nat. Phys.* https://doi.org/10.1038/s41567-023-02059-7 (2023).

Publisher's note Springer Nature remains neutral with regard to jurisdictional claims in published maps and institutional affiliations.

Methods

Femtosecond electron pulse generation in a transmission electron microscope

The experimental work was carried out in two commercially available transmission electron microscopes (JEOL JEM 2100F and JEM F200) that have been modified to allow the investigation of ultrafast dynamics in a stroboscopic laser-pump/electron-probe measurement scheme[16]. As our electron source, we employ W(100)/ZrO Schottky emitters (radius of curvature $r = 490$ nm, ~100 nm physical emission size) operated at $U_{ext} = 0.4$–2.1 kV and a bias voltage of $U_{bias} = -0.3$ kV. After cooling the W(100)/ZrO emitter to just below the continuous Schottky emission threshold (filament current 1.6 A), the work function is close to the photon energy of the laser ($E_{ph} = 2.4$ eV, corresponding to a 515 nm central wavelength). We generate ultrashort electron pulses via close-to-threshold linear photoemission by focusing laser pulses (160 fs pulse duration, 600 kHz/2 MHz repetition rates, 30 μm × 20 μm spot size) onto the apex of the nanotip. Apertures in the electro-optical beam path limit the transmitted beam to electrons that were generated close to the optical axis, resulting in average transmitted bunch charges of below one electron per pulse. Subsequent acceleration to 200 keV energies and coupling to the microscope column enables a pulse characterization in real and reciprocal space; spectral pulse properties are studied using an imaging energy filter (CEFID, CEOS).

Event-driven photoelectron detection

The correlated photoelectron states are imaged with a hybrid pixel electron detector based on the Timepix3 ASIC (EM CheeTah T3, Amsterdam Scientific Instruments) and mounted behind the imaging energy filter. The camera generates a stream of data packages containing the position of electron-activated detector pixels, their times of arrival (digitized with 1.56 ns time bins) and the energy (time-over-threshold, TOT) associated with incident electron events. At a beam voltage of 200 kV every individual electron activates a cluster of pixels of variable size ($N_{pixels,avg} \approx 8$ pixels), shape and energy ($TOT_{avg} \approx 280$ a.u.).

Single-electron-event localization of the TOT-corrected raw data stream is achieved using the Division of Nanoscopy, M4I, Maastricht University event clustering code[74,75], which is based on a hierarchical density-based spatial clustering in Python3. The algorithm reconstructs the timing and position of individual electrons incident on the detector from the activated pixels. Individual electrons are thereby distinguished in terms of their times of arrival, attributing between three and nine neighbouring pixels activated within a time window of 100 ns and a summed TOT ranging from 200 a.u. to 400 a.u. for the same cluster (see ref. [74]).

In a second step, the photoelectrons are clustered according to the femtosecond laser pulse that generated them. The temporal resolution of the detector (1.56 ns) is much faster than the temporal pulse separation given by the laser (500 ns and 1.6 μs for repetition rates of 2 MHz and 600 kHz), but much slower than the temporal splitting of the correlated electrons at the detector (~1 ps). The electrons arriving at the detector within $\Delta t_n = 50$ ns are thus assigned to a number-class electron state $n = 1, 2, 3, \ldots$ determined by the number of electrons per laser pulse. The length of the electron correlation time window Δt_n is chosen to capture all correlated electrons while being much shorter than the dead time between laser pulses (Supplementary Section A).

Effect of stochastic Coulomb interactions and the mean field on few-electron states

Even though only a fraction of electrons generated at the emitter surface is transmitted to the microscope column[17], the spatiotemporal confinement of the emission results in a non-negligible influence of the entire electron cloud on the properties of the transmitted beam. Consequently, mean-field (space charge) and stochastic interactions between all electrons both need to be considered and distinguished from

the correlations observed in the electron pair state. These different contributions can be assessed by laser-power-dependent measurements. The corresponding $n = 1$ and $n = 2$ spectral distributions, as well as the $n = 2$ average pair energy $(E_A + E_B)/2$ (Extended Data Fig. 2a,b,d), display the expected broadening with increasing laser power (compare Extended Data Fig. 2e; $n = 1$ broadening (orange circles) and average pair energy broadening (grey circles)) that scales with the average photocurrent. This is in close correspondence to previous non-event-selective measurements[17,35,65] and is typically attributed to stochastic Coulomb interactions and mean-field effects.

In contrast, the two-electron correlation functions displayed in Extended Data Fig. 2c are remarkably independent of laser power, showing a pronounced gap that is about 1 eV wide, a peak at around 1.8 eV and an extended tail towards large energy separations exceeding 4 eV. Increasing the photocurrent only imposes moderate variations in the depth of the gap and the shape of the high-energy tail. In particular, the position of the main correlation peak (Extended Data Fig. 2e, blue circles) approaches a fixed value of 1.7 eV towards small average currents, demonstrating that the observed correlation is only weakly altered by multiple Coulomb interactions with the space-charge cloud. The peak position is instead dominated by the two-electron correlation.

State-averaged energy-subtracted spectra

Shot-to-shot variations between electron pulses deteriorate the state-averaged (Extended Data Fig. 1a) and number-state resolved (Extended Data Fig. 1b–e) spectra. They are primarily caused by high-voltage and space-charge fluctuations that change $\bar{E}$. As a result, the characteristic multi-peak spectra of the few-electron states are blurred, particularly for electron states with $n \geq 2$. Correcting every individual pulse for $\bar{E}$ thus substantially enhances the visibility of the multi-peak spectra (compare Extended Data Fig. 1f–h). The root-mean-square widths of the state-average energies shown in Extended Data Fig. 1i–k are reduced for higher number states ($n = 2, 3, 4$: 0.73, 0.6, 0.52 eV).

Two-laser-pulse electron generation

For the two-laser-pulse generation described in Fig. 2g, a Michelson interferometer splits the incoming laser pulse into two separate pulses. One of the interference arms has a variable optical path length, implemented by a retroreflector mounted on a delay stage. The delay time of the two optical pulses (up to 2 ps) is much shorter than the laser pulse repetition time (1.6 μs, corresponding to a repetition rate of 600 kHz). Hence, two photoelectrons generated by two separate laser pulses and two photoelectrons generated by the same pulse are both detected as two-electron events.

As the optical power on the tip oscillates for small delay times due to constructive and destructive interference of the laser pulses, the number of generated electrons strongly varies in this delay regime. Therefore, we select delays with approximately the same one-electron-state rate ($\pm\sigma/2$) over the integration time of 5 s (see Supplementary Section B for a detailed description of the data selection).

Numerical simulations of multi-particle trajectories

Energy correlation histograms for the electron number states $n = 2$–4 are shown in Fig. 2b–d. These correlation spectra are reproduced with the numerical multi-particle trajectory simulations discussed in Fig. 2e–h and in Supplementary Section C. For the simulation of the $n = 3, 4$ correlation spectra, the model is extended to three and four particles. We compute the electron trajectories of all n states for a set of parameters within the experimental range: an extraction voltage of 2,100 V, a temporal emission profile of 180 fs, a physical source size of 100 nm and considering the mean-field broadening of 1 eV observed for the $n = 1$ state. The simulated multi-particle energy-pair histograms are shown in Extended Data Fig. 3d–f and are in excellent agreement with the experimental data (Extended Data Fig. 3a–c) in terms of the observed correlation gaps and peak positions.

Data availability

Source data are provided with this paper. These data are also available via Edmond[76]. All other data that support the plots within this paper and other findings of this study are available from the corresponding authors upon reasonable request.

References

74. van Schayck, J. P. et al. Sub-pixel electron detection using a convolutional neural network. *Ultramicroscopy* **218**, 113091 (2020).
75. van Schayck, J. P. M4I-nanoscopy/tpx3HitParser: version 2.1.0. *Zenodo* https://doi.org/10.5281/zenodo.4580458 (2021).
76. Haindl, R. et al. Figure source data supporting "Coulomb-correlated electron number states in a transmission electron microscope beam. *Edmond* https://doi.org/10.17617/3.VQZOV7 (2023).

Acknowledgements

Author contributions

Conceptualization: C.R. directed the study, which was conceived by C.R. and A.F. The experiments were conducted by R.H., with support from A.F. The data were analysed by R.H. and A.F., with support from M.M. The figures were prepared by R.H., with contributions by T.D. and S.V.Y. The electron gun was modified and characterized by R.H. and J.H.G., with support from M.M. and A.F. Particle simulations were conducted by S.V.Y. and R.H., with support from T.D., A.F., and C.R. All authors discussed the results and interpretation. The manuscript was written by R.H., A.F., and C.R., with contributions by S.V.Y., and input and feedback from all authors.

Funding

Competing interests

A.F., R.H. and C.R. are named inventors on a patent application (European patent application no. 22197542, filed by the Max-Planck-Gesellschaft zur Förderung der Wissenschaften e.V.) related to technology presented in this manuscript. All other authors declare no competing interests.

Additional information

Extended data is available for this paper at https://doi.org/10.1038/s41567-023-02067-7.

Supplementary information The online version contains supplementary material available at https://doi.org/10.1038/s41567-023-02067-7.

Correspondence and requests for materials should be addressed to Armin Feist or Claus Ropers.

Peer review information *Nature Physics* thanks Kasra Amini, Phillip Keathley and the other, anonymous, reviewer(s) for their contribution to the peer review of this work.

**Reprints and permissions information** is available at www.nature.com/reprints.
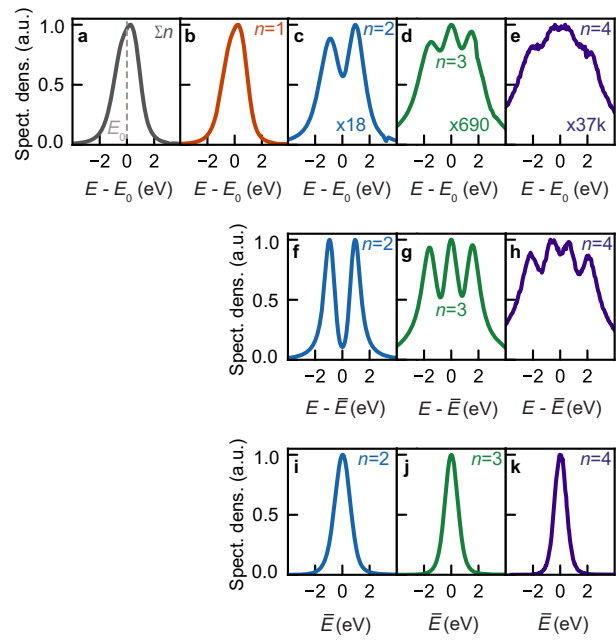
Extended Data Fig. 1 | State-average energy subtracted electron spectra. The event-averaged spectrum with a rms energy spread of 1.08 eV (**a**) is separated into number-state resolved contributions ($n = 1 – 4$: **b-e**). Voltage- and space charge-fluctuations smear out the characteristic n-peak spectra. **f-h**, For $n = 2 – 4$, the state-average energy $\bar{E}$ is subtracted from the n-state energies and the $\bar{E}$-corrected n-spectra are plotted. **i-k**, Plot of the state-average spectra for $n = 2 – 4$ with a rms energy spread of $n = 2$: 0.73 eV, $n = 3$: 0.60 eV, $n = 4$: 0.52 eV.
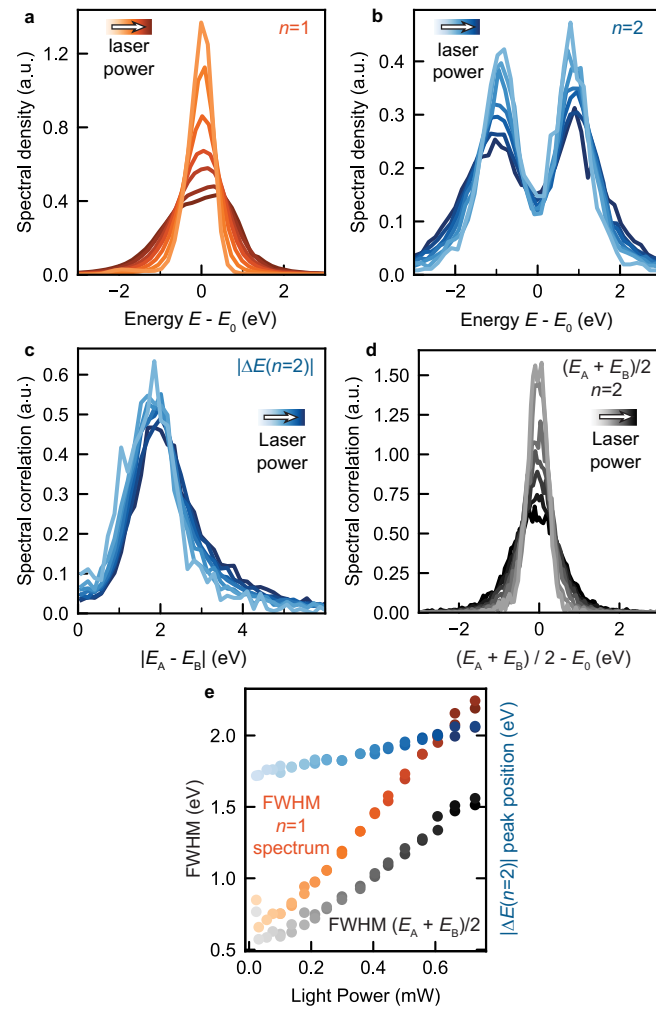
Extended Data Fig. 2 | Effect of stochastic Coulomb interactions and space charge on few-electron states. a, b, Normalized $n = 1$-spectra (**a**) and $n = 2$-spectra (**b**) for varying laser power. **c, d**, Normalized one-sided pair correlation functions (**c**) and pair distributions in average energy $(E_A + E_B)/2$ (**d**) (both for $n = 2$) for varying laser power. **e**, Power scaling of the peak position of the $n = 2$-correlation function compared to the spectral width (FWHM) of the $n = 1$-state and of the electron pair average energy.
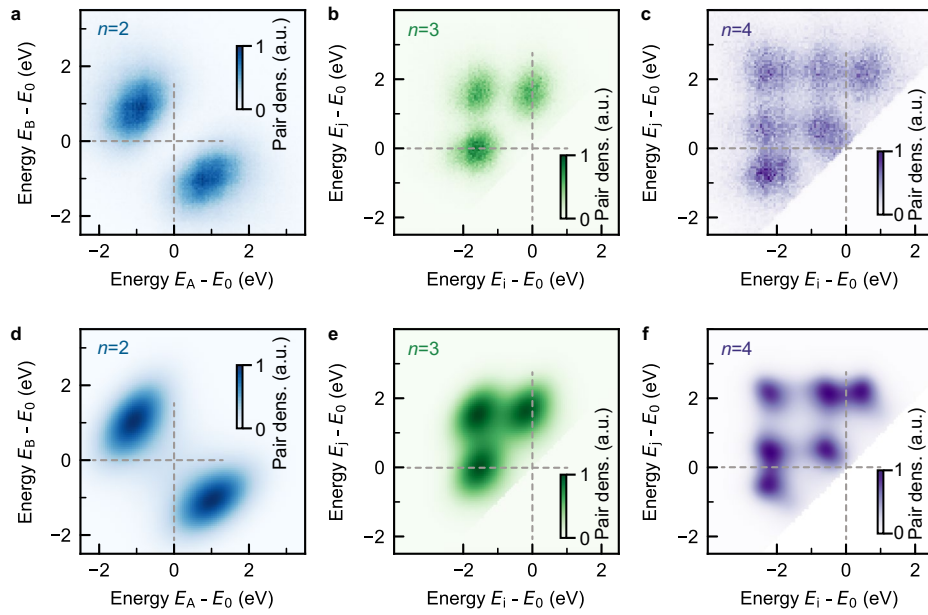
Extended Data Fig. 3 | Numerical simulations for double-, triple- and quadruple-states. The experimental sorted energy histograms of the $n = 2 - 4$-states (**a-c**) are compared with multi-electron energy histograms from the particle trajectory simulation (**d-f**: $n = 2 - 4$). The energy-pair correlation peaks are clearly resolved and in excellent agreement with the experimental data.
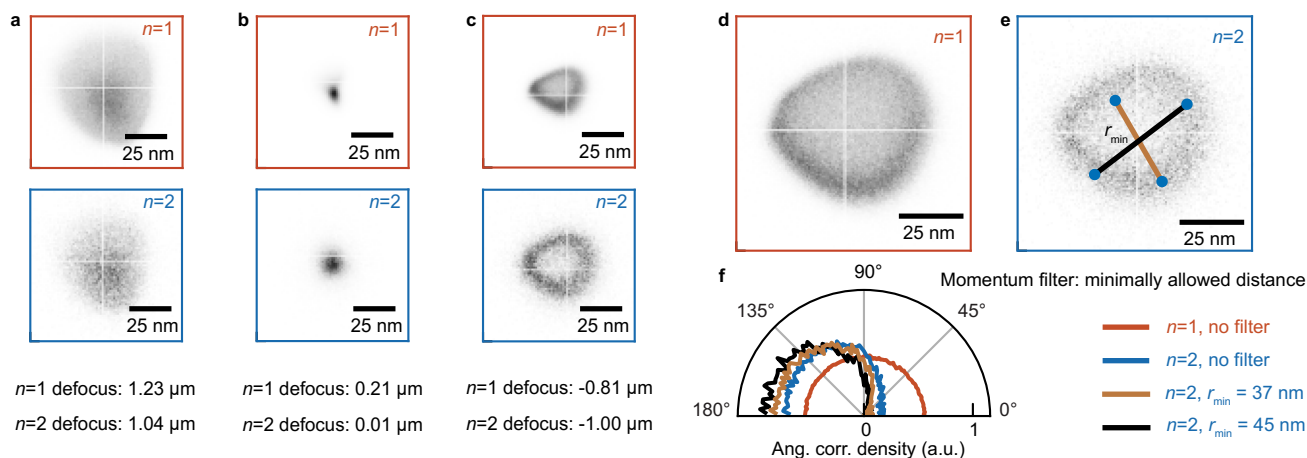
Extended Data Fig. 4 | Comparison of beam profiles and transverse momentum filters. a-c, Beam profiles of $n = 1$- and $n = 2$-states in overfocus (**a**), focus (**b**) and underfocus (**c**) condition. The beam profiles of both number classes agree qualitatively considering the Coulomb-correlation-induced defocus shift and increase in spot size. **d, e**, Underfocus $n = 1$- and $n = 2$-beam profiles used in the angular correlation analysis in Fig. 4d in the main text. **e**, Digital transverse momentum filters are plotted in brown and black onto the $n = 2$-beam profile. The filters only consider electron pairs where both electrons have a minimum distance r_{min} to each other. **f**, Plot of the angular correlation density without filter for $n = 1, 2$ (red and blue) and with filter for $n = 2$ (brown: $r_{min} = 37$ nm and black: $r_{min} = 45$ nm). The distribution for $n = 2$ becomes increasingly more pronounced at 180° after application of the transverse momentum filters.